Transmission Computed Tomography Imaging of the Head with a SPECT System and a Collimated Line Source

Brad J. Kemp, Frank S. Prato, Richard L. Nicholson and Lionel Reese

Department of Nuclear Medicine and Magnetic Resonance, St. Joseph's Health Centre, Lawson Research Institute and The University of Western Ontario, London, Ontario, Canada

Transmission images of relatively high resolution as compared to SPECT are needed for brain SPECT quantification to provide skull thickness, attenuation coefficients and anatomical correlation. Consequently, a technique to acquire transmission CT images with a SPECT system by using a collimated line source positioned at the focal line of a fanbeam collimator (FBC) has been developed. **Methods:** Computer simulations that model the transmission imaging system optimized the system resolution and tested the validity of a equation for the geometric efficiency of the line source collimator (LSC). Based on the computer simulations, a LSC was constructed with tantalum septa 100 mm long, 0.5 mm thick and spaced 1.0 mm apart. A 600-mm focal length FBC was used. Experiments were conducted to measure the system resolution and to determine the effect of the LSC on the amount of detected scatter. **Results:** The simulations showed that without a LSC the transmission images have a longitudinal resolution (LR) characterized by the resolutions of the FBC (depth-dependent, ~8 mm FWHM at 150 mm) and the detector (~4 mm). However, with an optimally designed LSC, the contribution of the FBC to the system resolution can be made negligible, creating a system with a LR that is comparable to the detector resolution and independent of object depth. Resolution experiments conducted with a lucite rod phantom showed that the LR and TR are better than 4.8 mm and confirmed the results of the computer simulations. **Conclusion:** Brain transmission images of relatively high isotropic resolution can be obtained using a SPECT system, a FBC and an optimized LSC.

Key Words: line source collimator; transmission imaging; attenuation correction

Attenuation is a major limitation preventing SPECT from accurately quantifying organ function. However, it is difficult to compensate SPECT images for attenuation since the source is of unknown strength and distribution

and is located in a medium of unknown composition. There are many attenuation corrections that assume the body is homogeneous and therefore employ a constant attenuation coefficient (*1–6*). These algorithms will not accurately correct SPECT images of the chest (*7,8*) or the brain (*9*) for attenuation where there is more than one media present. In order to provide accurate attenuation correction, the attenuation coefficients of the body must be known. Transmission computed tomography (TCT) images show anatomic structures and are a map of the attenuation coefficients of the body. The attenuation coefficients of a TCT image can be used to correct the SPECT image for attenuation, therefore improving the accuracy of the quantifications.

Accurate quantification of functional images also implies that the precise location of the radiopharmaceutical can be identified. Anatomic orientation is facilitated by superimposing or correlating the functional images to the anatomic images (*10–13*), but the poor resolution and high noise of the SPECT images limit the accuracy of the correlations. TCT combined with x-rays produces images of high quality and resolution but requires the transfer of the TCT and SPECT datasets to a workstation where sophisticated software correlates the images. A SPECT system can also be used to acquire the transmission images, either simultaneously with the emission study (*16,22,27*), or sequentially prior to the emission study (*8,14,15,17–21,23–26*). Image correlation is simplified as both image datasets are automatically registered and located on the same computer provided the patient does not move between the TCT and SPECT acquisitions. Three source-collimator configurations for TCT imaging with a SPECT system have been proposed: a sheet source and a parallel-hole collimator (*14–18*), a point source and a conebeam collimator (*19–21*) and a line source and a fanbeam collimator (*22–26*).

Parallel-beam CT consists of placing a sheet source opposite a SPECT detector equipped with a parallel-hole collimator (PHC). The sheet source may be collimated to reduce the dose to the patient and the amount of detected scatter, and to improve the spatial resolution (*18*). The resolution of the TCT images, typically 9–10 mm, is sufficient to delineate large regions such as the lung but does not permit measurement of skull thickness. A scanning line

source opposite a PHC has been proposed as a replacement for the sheet source (27). This approach reduces the scatter content of the transmission images but does not improve upon the resolution.

Transmission CT imaging with a point source at the focal point of a conebeam collimator (CBC) acquires images with high resolution in the transverse and longitudinal directions (19–21); the longitudinal direction being coincident to the axis of rotation of the SPECT detector. This technique uses a low-activity source but it suffers from image truncation and undersampling of the object being imaged.

Another approach is to acquire TCT images with a line source at the focal line of a fanbeam collimator (FBC) (22–26). The FBC provides transmission images with the resolution of a CBC in the transverse direction and a PHC in the longitudinal direction. As such, the resolution of the images in the transverse direction is sufficient to resolve the skull thickness but the poor resolution in the longitudinal direction exaggerates partial volume effects and produces incorrect measurements of the attenuation coefficients (28). Partial volume effects are prevalent in head images where the structure is small and can be reduced by improving the system resolution. The notion of a line source collimator (LSC) has been proposed by Jaszczak (24), and we have introduced a LSC that improves the resolution in the longitudinal direction (25,26). The focus of this paper is the optimization of the design of a LSC to be used in a transmission imaging system comprised of a SPECT detector and a fanbeam collimator. The characterization of the resolution and geometric efficiency of the transmission imaging system and an investigation of the ability of the system to measure narrow-beam attenuation coefficients in both phantoms and a human head are presented.
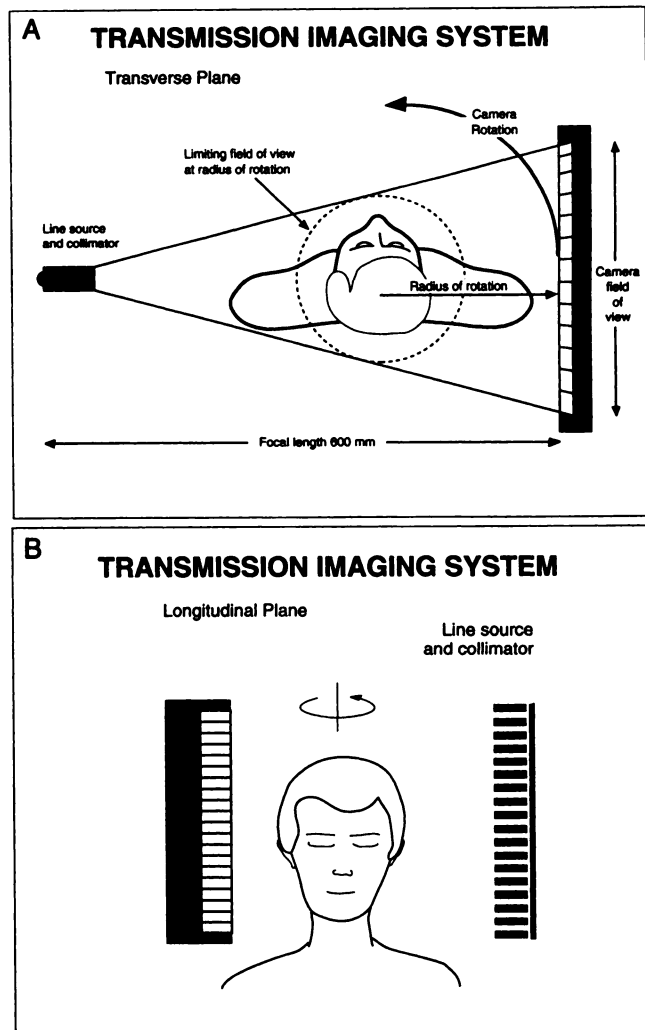
MATERIALS AND METHODS

Transmission Imaging System

The transmission imaging system consists of a collimated line source at the focal line of a FBC. The LSC is a one-dimensional collimator with septa that are stacked in the longitudinal direction. The system is shown in the transverse and longitudinal directions in Figures 1A and 1B, respectively.

Computer Simulations

Computer simulations were used to evaluate different LSC designs by measuring both resolution and geometric efficiency when the LSC septal length and spacing were varied. To calculate the system resolution, transmission projections of a flat, rectangular attenuating block were simulated. The simulations were Monte Carlo ray tracings that modeled the transmission imaging system. The code used the variance reduction technique of importance sampling (forced detection (29)); gamma rays were uniformly emitted along a ^{99m}Tc line source of finite length and diameter with a direction within the solid angle of the detector field of view (FOV). The line source was located at the focal line of the FBC. Each gamma ray was emitted with a history weight of one, which was adjusted by the probability that the gamma ray passed through the LSC and the block unattenuated. For a gamma

FIGURE 1. Schematic diagrams of the transmission imaging system. (A) transverse direction and (B) longitudinal direction. The system consists of a SPECT camera and a collimated line source that is located at the focal line of a FBC. The line source collimator (LSC) is a one-dimensional collimator with septa that are stacked in the longitudinal direction.

ray to be detected, it had to pass unattenuated through an FBC hole of specified size and shape. Septal penetration in the FBC was implicitly modeled through the use of an effective hole length, $l_e = l - 2/\mu_{Pb}$ (30), where l and l_e are the true and effective hole lengths, respectively, and μ_{Pb} is the linear attenuation coefficient for the lead FBC. The attenuation coefficients for the attenuating block and the line source and FBCs were obtained from NIST software (31). The simulations also modeled the intrinsic resolution of the detector as a symmetric Gaussian distribution. The history weight of the gamma ray was added to the appropriate element of the acquisition matrix. Trajectories are followed for an ensemble of gamma rays until a preset average in the background region was obtained. The simulations were run for the following collimator configurations: with the FBC without the LSC (wFBCwoLSC), without the FBC with the LSC (woFBCwLSC), and with the FBC with the LSC (wFBCwLSC).

All simulations were run on an nCUBE 32 node parallel processor (nCUBE Corporation, Foster City, CA). The images were then transferred to the GE STAR (General Electric, Milwaukee,

WI) environment for processing. Edge-spread functions (ESF) were obtained as thick profiles through the block in the longitudinal and transverse directions. The ESFs were differentiated to produce line-spread functions (LSF) and the corresponding FWHM in the longitudinal and transverse directions were used as a measure of the spatial resolution.

For the simulations, a 600-mm focal length FBC with hexagonal holes 1.5 mm (flat-to-flat) wide and 40 mm in length and a septal thickness of 0.25 mm was modeled. The intrinsic resolution of the detector was fixed at 3.8 mm. The line source was 120 mm long and 1 mm in diameter. The LSC septa were constructed of 0.5-mm thick tantalum plates with variable length and spacing. The attenuating block was made of tantalum 20 mm long and 0.5 mm thick and was placed at distances of 50, 100, 150 and 200 mm from the FBC. The acquisition matrix was 128 × 128 with a 5.33 zoom (1 pixel = 0.60 mm). The small pixel size oversamples the LSF and eliminates the need to slant the attenuating block as suggested by Judy (32) or to correct for the aliasing introduced by the discrete differentiation (33). The projections contained sufficient counts to minimize the noise in the LSF (34).

Geometric Efficiency of the LSC

The geometric efficiency of the LSC, G_{LSC}, can be defined as

$$G_{LSC} = \frac{L_{OPEN}}{L_{UNIT}} \times \frac{\Omega}{4\pi} = \frac{S_{LSC}}{S_{LSC} + t_{LSC}} \times \frac{S_{LSC}}{2\pi l_{LSC}}, \qquad \text{Eq. 1}$$

where L_{OPEN}/L_{UNIT} is the fraction of the line source unobstructed by the LSC and Ω is the solid angle of the LSC. The LSC septa have length l_{LSC}, thickness t_{LSC}, and are separated by a distance S_{LSC}. A complete derivation of the equation is located in the Appendix. To verify the equation, the computer simulations tabulated the number of emitted gamma rays that pass through the LSC unattenuated as the length, thickness and spacing of the LSC septa were varied.

LSC Construction

Based on the simulations, a LSC was constructed with tantalum septa 100 mm long, 0.5 mm thick and spaced 1.0 mm apart. Tantalum (Ta, z = 73) is an inert metal that is a better attenuator than lead (μ_{Ta} = 30.3 cm^{-1}, μ_{Pb} = 27.2 cm^{-1}) at 140 keV (31). It has the mechanical properties of mild steel and is more rigid than lead. Therefore the septa do not need to be sandwiched between spacing material (24). The longitudinal length of the LSC was 210 mm. The line source (Data Spectrum Corp., Hillsborough, NC) was located at the FBC focal length and shielded by 6 HVLs of lead on all sides except the LSC side. The LSC was attached to the FBC by a tripod fastened directly to the collimator ring. To enable the detector to rotate by overcoming the moment (torque) of the LSC, a counterweight was mounted 300 mm above the camera counterweight on the side opposite the LSC, as shown in Figure 2.

Transmission Acquisitions

Resolution Experiments. The system resolution was evaluated in the transverse and longitudinal directions by using a plastic rod phantom (Deluxe Model 5000, Data Spectrum Corp., Hillsborough, NC). The rods are arranged in six pie-shaped sectors, with each sector having 88-mm long rods of the same diameter. The rod diameters are 4.8, 6.4, 7.9, 9.5, 11.1 and 12.7 mm, and the center-to-center spacing between the rods is twice the diameter. To evaluate transverse resolution, the phantom was oriented with the rods parallel to the axis of rotation (AOR) of the detector. Conversely, to evaluate the longitudinal resolution, the phantom was
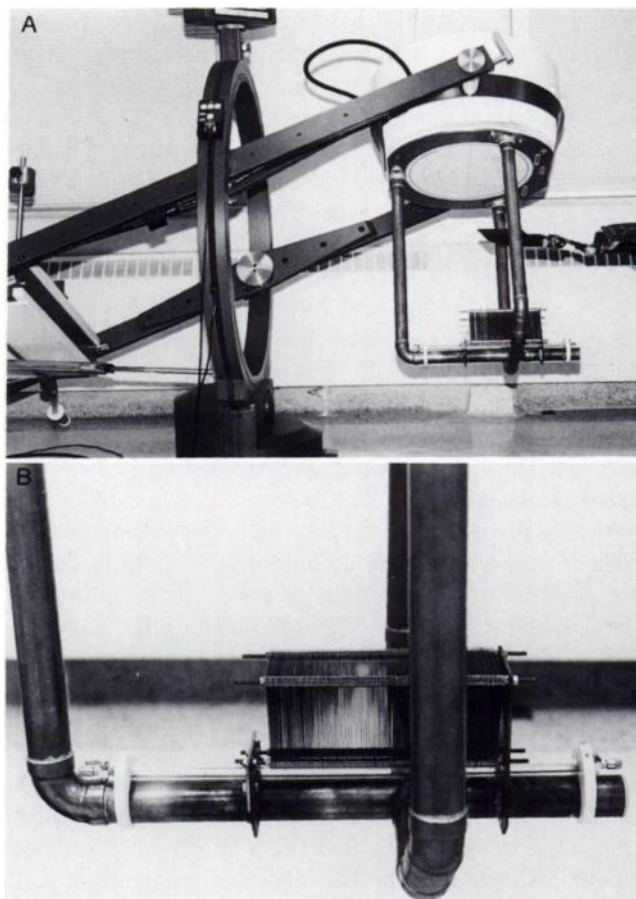
FIGURE 2. (A) The transmission system and (B) a close-up of the LSC. The line source can be removed easily by unfastening the two teflon collars. The lead shielding for the line source is not present.

oriented with the rods perpendicular to the detector AOR. The phantom was imaged for the collimator configurations wFBCwoLSC, woFBCwLSC and wFBCwLSC with line source activities of 60 MBq, 80 MBq and 400 MBq of ^{99m}Tc, respectively. The count rates did not exceed that which would produce a 8% deadtime loss ($\leq$27,000 cps), and the mean background count density for all collimator configurations was 150 counts per pixel per projection. The time per projection was adjusted to give the same total counts in the first projection for all configurations. A SPECT system (Camstar 400AC, General Electric, Milwaukee, WI) was used to acquire 128 projections equally spaced over 360° into 128 × 128 matrices (1 pixel was 3.2 mm on edge, excluding magnification). The SPECT system was equipped with an FBC with a focal length of 600 mm, a hole length of 40.0 mm, a hexagonal hole width of 1.5 mm and a septal thickness of 0.25 mm (Nuclear Fields Corp., Des Plaines, IL). For the collimator configuration, woFBCwLSC, the LSC holder was attached to a collimator ring that had the septa removed. The radius of rotation was 140 mm. An energy window of 20% centered on the ^{99m}Tc photopeak was used. All projections were corrected using linearity and energy correction files. Single blank projections (without the phantom) were also acquired for each collimator configuration. The blank projections were 128 × 128 matrices with 30 million counts. After reconstruction, high-count transverse and sagittal images were created by summing thirty slices together.

Scatter Experiments. Tomographic acquisitions of a 160-mm diameter water phantom were acquired with and without the LSC (wFBCwLSC and wFBCwoLSC) to investigate the scatter content of the transmission images. The ^{99m}Tc source activities were 900 and 160 MBq with and without the LSC, respectively, and the imaging parameters were the same as for the resolution experiments. The radius of rotation was 150 mm. A 30-million count blank projection was also acquired. For the two collimator configurations, a reconstructed slice 130 mm thick was created, through which a 10-mm thick profile was drawn. Also, the mean attenuation coefficient in a large ROI (1500 pixels) drawn in the center of the images was obtained and the error expressed as the standard deviation of the attenuation coefficient.

Human Head Experiment. The transmission imaging system (wFBCwLSC) was used to acquire images of the head of a human volunteer. The imaging parameters were the same as that for the resolution experiments. A 1100-MBq ^{99m}Tc source was used. The count rate was 32,000 counts per second and the background count density was 300 counts per pixel per projection. The radius of rotation was 190 mm and the total imaging time was 42 min. A 50-million count blank projection was also acquired. Transverse slices 1 pixel thick (2.0 mm) were created. The mean attenuation coefficients of the brain tissue and bone were measured from ROIs drawn on five transverse images. The error is expressed as the mean standard deviation of the attenuation coefficients within the ROIs.

Reconstruction

The transmission projections were converted into attenuation projections using the equation

$$\mu_m(i, j) = \ln [N_0(i, j)/N_m(i, j)] \cdot C, \qquad \text{Eq. 2}$$

where μ_m is the line integral of the attenuation coefficients of the object at angle m; $N_0(i, j)$ is the blank projection; $N_m(i, j)$ is the transmission projection; C is a scaling constant; and (i, j) is a pixel in the projection matrix. The background region of N_m was scaled to N_0 and was corrected for source decay during the acquisition and for the center of rotation offset. The normalization of the blank projection to the transmission projection will correct for nonuniformities in the projections. In addition, the blank projection contained sufficient count density to minimize the statistical errors in the normalization (35).

The attenuation projections were reconstructed using a fanbeam, filtered backprojection algorithm (Fanbeam Prototype Research Software, IGEMS Nuclear Medicine, Radlett, UK) based on the method proposed by Gullberg (36). The algorithm requires integer projections, hence C scales the attenuation projections to avoid integer truncation. It was found that a value of 100 was appropriate. A Hann prefilter with a cutoff at the Nyquist frequency was used. For the human head experiment, the filter cutoff was set to 85% of the Nyquist frequency to provide greater image smoothing.

RESULTS

The longitudinal resolution of the system, measured from the simulations of a thin block 150 mm above the FBC, is plotted as a function of the LSC septa length in Figure 3. The longitudinal resolution for collimator configuration wFBCwoLSC is equal to the combined FBC and the intrinsic detector resolutions (8.1 mm). This is shown at a septal length of zero, but is extended for reference. In the
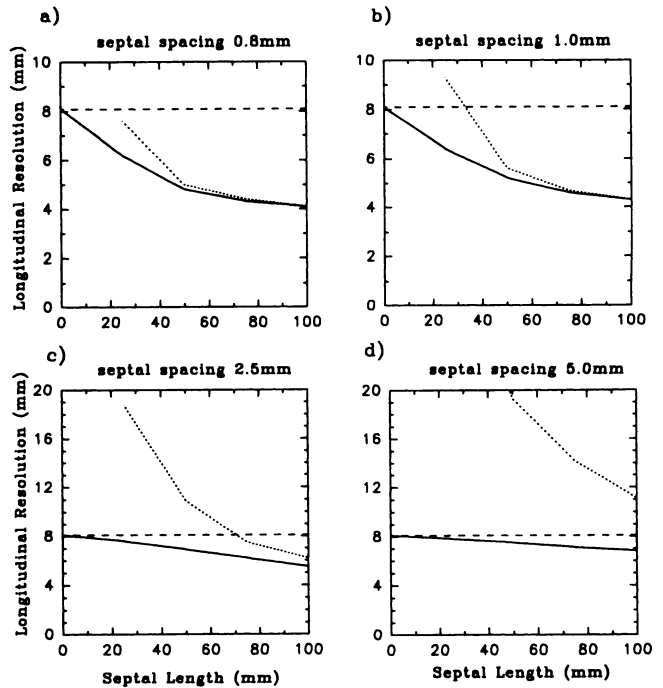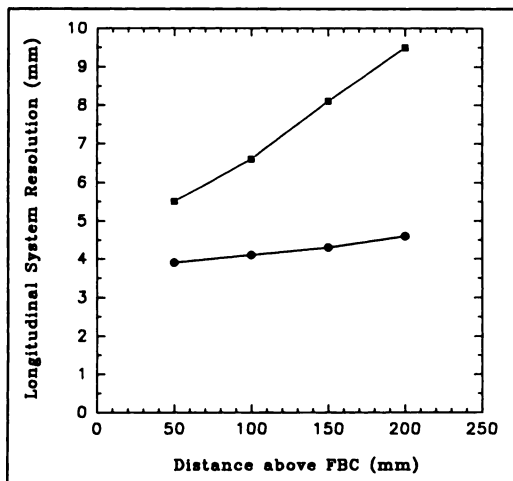

FIGURE 3. Computer simulation results showing the longitudinal resolution (LR) of the system as a function of the line source collimator septal length. The septal spacing is (a) 0.8 mm, (b) 1.0 mm, (c) 2.5 mm and (d) 5.0 mm. The septal thickness is 0.5 mm and the intrinsic detector resolution is 3.8 mm. Solid line: wFBCwLSC; dashed line: wFBCwoLSC; dotted line: woFBCwLSC. Note that the LR increases as the septal length increases and the septal spacing decreases. For long septal lengths and small septal spacings the resolution of the collimator configuration woFBCwLSC approaches that of wFBCwLSC.

longitudinal direction without the LSC, the FBC behaves as a parallel-hole collimator. The longitudinal resolution of the imaging systems with the LSC (woFBCwLSC and wFBCwLSC) improves as the LSC septa length increases and the septal spacing decreases. The gamma rays are focused into a thin fan in the transverse plane; an increase in septal length or a decrease in septal spacing reduces the solid angle of the LSC and improves the longitudinal resolution. In the limit of an LSC with long septal lengths and small septal spacings the system resolution is equal to the resolution of collimator configuration woFBCwLSC; the contribution of the FBC to the system resolution is negligible.

The longitudinal resolution is dependent on the FBC and LSC resolutions, both of which are dependent on the object depth. For a high-resolution LSC, the dependence of the system resolution on object depth is diminished; the FBC contribution to the system resolution is negligible and the LSC dependence on object depth is reduced. This is illustrated in Figure 4 for the transmission system without an LSC and with an LSC with septa 100.0 mm long, 0.5 mm thick and spaced 1.0 mm apart.

The computer simulations also show that the transverse resolution is equal to the intrinsic detector resolution (3.8 ± 0.1 mm s.d.), independent of the collimator configuration and the object distance above the detector. The
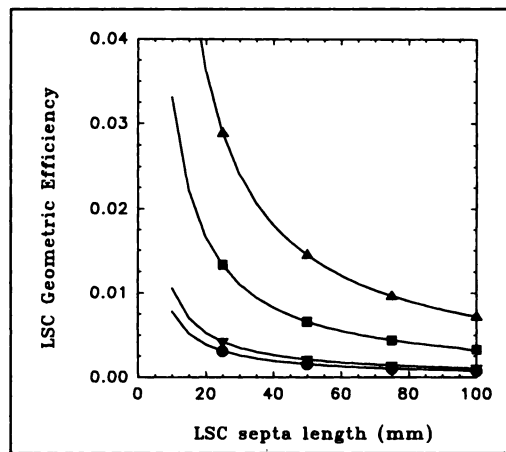
FIGURE 4. Computer simulations showing the longitudinal system resolution as a function of distance above the FBC. Circle: wFBCwLSC, where the LSC had septa 100.0 mm long, 0.5 mm thick and spaced 1.0 mm apart; squares: wFBCwoLSC. The dependence of the system resolution (wFBCwLSC) on depth is diminished as the contribution of the FBC has been removed by the LSC.

FIGURE 5. The geometric efficiency of the LSC as a function of septal length. The line represents the geometric efficiency calculated using Equation 1 and the symbols represent the geometric efficiency measured using the computer simulation for different septal spacings. Triangle: 5.0 mm; square: 2.5 mm; inverted triangle: 1.0 mm; and circle: 0.8 mm. The septal thickness is fixed at 0.5 mm. The results show that the geometric efficiency can be calculated using Equation 1.

effect of the FBC is removed from the transverse resolution because the source is located at the focal line. As a result, the transverse resolution is characterized by the source distribution and the intrinsic detector resolution (37). However, our system uses a small diameter line source, and the effect of the source distribution is negligible. Therefore, the transverse resolution is effectively equal to the intrinsic detector resolution.

The geometric efficiency of the LSC is plotted as a function of septal length in Figure 5. The efficiency decreases as the solid angle of the LSC decreases, with the solid angle proportional to the septal spacing and inversely proportional to the septal length. The computer simulations confirm that the efficiency can be calculated using Equation 1.

Based on the results of the computer simulations, an LSC design that creates an imaging system with near isotropic resolution was constructed. Due to construction limitations, we set the septal thickness to 0.5 mm, although thinner septa would be preferred. Simulations then confirmed that an LSC with 100 mm septal length and 1 mm septal spacing would provide the desired longitudinal resolution while maximizing the geometric efficiency at 0.1%.

The results of the resolution experiments are shown for the transverse and longitudinal directions in Figures 6A and 6B, respectively. Each figure contains images of the Lucite rod phantom for the three collimator configurations. In the transverse direction, all sectors, including the 4.8-mm diameter rods, are resolved for all three collimator configurations, implying that the transverse resolution is better than 4.8 mm, as predicted by the computer simulations. In the longitudinal direction, the collimator configuration wFBCwoLSC resolves the 6.4-mm rods but some streak artifacts are present. For the collimator configurations with the LSC, namely woFBCwLSC and wFBCwLSC, the 4.8-mm rods are re-

solved. These experiments confirm the computer simulations: the LSC improves the longitudinal resolution of the system, for an LSC with long septa and small septal spacings, the contribution of the FBC to the system resolution becomes negligible and our LSC creates an imaging system with near isotropic resolution (3.8 mm in the transverse direction and 4.3 mm in the longitudinal direction, as measured from simulations). For completeness it should be noted that the simulations calculate the resolution of the transmission projections, not the reconstructed transmission images and therefore do not consider the response of the reconstruction algorithm.

The attenuation coefficients measured from the water phantom experiment are listed in Table 1. The values are independent of the LSC and are equal to the narrow-beam water attenuation coefficient of 0.154 cm^{-1} at 140 keV (31). The equality of the water attenuation coefficients for the transmission system with and without the LSC is further illustrated by the profiles through the reconstructed transmission images of the water phantom, as shown in Figure 7. The profiles are square, flat, and have the same amplitude. The presence of scatter in the projections would produce a cupping artifact in the center of the images (or profiles) since scatter falsely increases the counts in a projection and makes the object appear less attenuating (38).

The presence of the LSC creates tantalum characteristic x-rays of 57.5 keV (39). With a high-activity source, the tantalum x-rays create pulse pileup, resulting in a loss of spatial resolution. Although the FBC does not contribute to the imaging system resolution, it attenuates most of the scatter and tantalum x-rays from the projections and should remain on the detector.

The transverse images of the human head are shown in
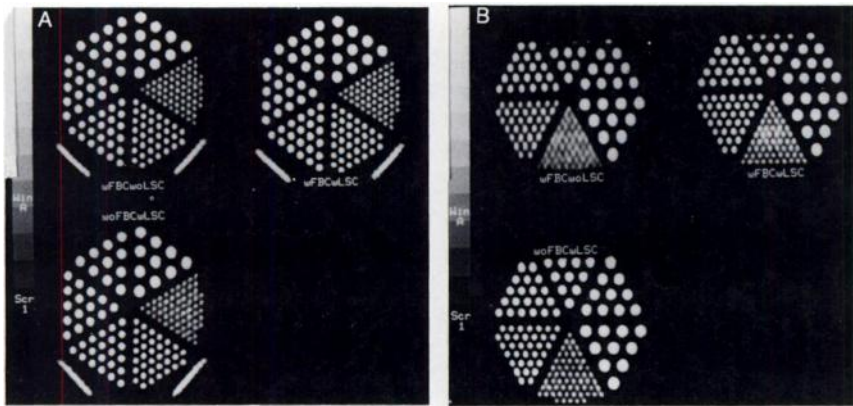
FIGURE 6. Transmission images of the Lucite rod phantom measuring resolution in the (A) transverse and (B) longitudinal directions. In each figure, the upper left quadrant is wFBCwoLSC, the upper right quadrant is wFBCwLSC and the lower left quadrant is woFBCwLSC. In the transverse direction all collimator configurations resolve the 4.8-mm diameter rods. In the longitudinal direction, only the collimator configurations with the LSC resolve the 4.8-mm rods.

Figure 8. The signal-to-noise ratio (SNR) in the tissue region is 15. The measured attenuation coefficients for the brain and bone tissues are shown in Table 1, and it is evident that the measured attenuation coefficients are within error of the narrow-beam attenuation coefficients (40). The resolution of the images is also apparent; the skull is visible, as are the frontal and sphenoid sinuses and the mastoid air cells.

DISCUSSION

We have designed and built a transmission imaging system that uses a SPECT system equipped with an FBC and a collimated line source. The fanbeam geometry is important for two reasons: it creates images with transverse resolution comparable to the intrinsic detector resolution and it magnifies the object in the image. The skull thickness is approximately 8–10 mm which requires a resolution of 4–5 mm in order to measure the thickness accurately (41). The intrinsic detector resolution is 3.8 mm and satisfies this criteria. The magnification is beneficial in the measurement of the skull thickness since it enlarges the object size with respect to the detector resolution. For a 600-mm FBC focal length and a 150-mm depth, the magnification is approximately 1.4, creating images with a skull thickness of 11–14 mm. The small anatomic structures of the head requires a SPECT transmission imaging system with the largest possible magnification. This statement is explained as follows: for transmission imaging systems, there is an optimum magnification (42); a large magnification enlarges the object with respect to the detector resolution to minimize the

effect of detector blurring, but it will also create a penumbra effect (blurring) from the source. The tradeoff is dependent on the detector resolution (3.8 mm) and the distribution of the source (focal spot diameter 1.0 mm). However, for transmission imaging with a SPECT system, the blurring due to the source is negligible when compared to the blurring by the detector. This results in an optimum magnification of 15 for our system $(1 + (3.8/1.0)^2$; equation 4.65 (42)) which is not possible to attain without severe image truncation. Hence, transmission imaging with a SPECT system requires as large a magnification as possible, without image truncation, to minimize blurring from the detector. The 600-mm focal length FBC is close to the minimum focal length permitted for our FOV detector without producing truncated projections of the head.

The longitudinal resolution of the transmission system, without the LSC, is characterized by the FBC and intrinsic detector resolutions. Our LSC has high resolution that effectively removes the contribution of the FBC from the system resolution. The high longitudinal resolution of the system (4.3 mm at 150 mm) is nearly independent of object

TABLE 1
Attenuation Coefficients Measured from Water Phantom and Human Head Images

	Water μ_w (cm^{-1})	Brain tissue μ_t (cm^{-1})	Bone (skull) μ_b (cm^{-1})
true (31,40)	0.154	0.159	0.246
wFBCwoLSC	0.152 ± 0.003*	—	—
wFBCwLSC	0.152 ± 0.003*	0.166 ± 0.014*	0.235 ± 0.014*

*s.d.
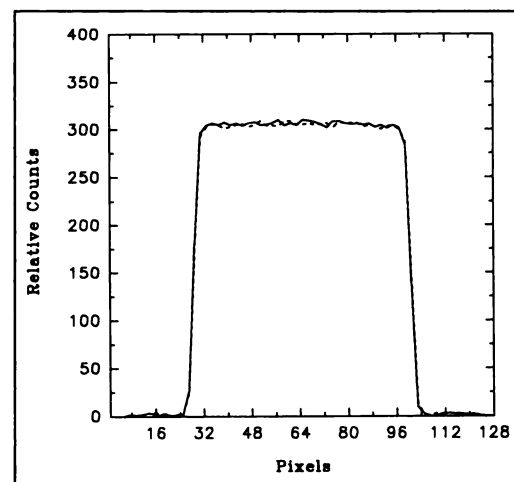
FIGURE 7. Profiles taken through a reconstructed transmission image of a water-filled phantom. Solid line: wFBCwLSC. Dashed line: wFBCwoLSC. From the shape and amplitude of the profiles it is concluded that there is negligible scatter content in the images, with or without the LSC.
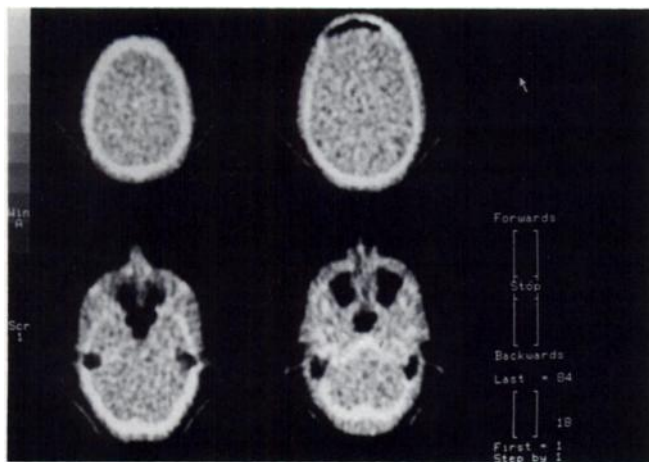
FIGURE 8. Transverse transmission images of a human head. Images show good contrast between bone and brain tissue. Spatial resolution is sufficient to resolve bony structure, sinuses and the head holder.

depth and increases the accuracy of attenuation coefficient measurement in objects whose structure varies longitudinally.

The geometric efficiency of the LSC is 0.001 and requires a high-activity source to produce images with an SNR greater than 15 in a reasonable acquisition time. However, the geometric efficiency of our LSC can be increased without sacrificing resolution. The septal thickness of 0.5 mm is 25 times thicker than that which is needed to produce 5% septal penetration (43). Although septa 0.02 mm thick are too fragile, a fourfold reduction in the septal thickness is feasible and would increase the geometric efficiency by 33%.

The SPECT system count rate capabilities and FOV were limitations of our transmission imaging system. The GE 400AC detector has a maximum count rate of ~105 kcps and a 20% count loss rate of 65 kcps. These performance specifications necessitated the use of a medium-activity source (<1200 MBq ^{99m}Tc) and, consequently, a long acquisition time was required to obtain images with an SNR of 15. If our transmission system is to be used in the clinical environment, the acquisition time must be reduced. Fortunately, state-of-the-art gamma cameras possess higher count rate capabilities and would permit a fourfold increase in the source strength and a corresponding decrease in the acquisition time. The GE 400AC detector also possess a 390-mm circular FOV which truncates the projections near the cerebellum region. A gamma camera with a large rectangular FOV would eliminate such image truncation.

The images of the human head show considerable detail. The measured attenuation coefficients for the brain tissue and bone are within experimental error of narrow-beam attenuation coefficients. Examination of the transverse images are a reminder that the head is not a homogeneous medium, and, if a uniform attenuation correction is used, the different anatomy will cause errors in the count densities of the cortical and cerebellar slices. Therefore, proper attenuation correction is required for both absolute and relative quantification of SPECT brain images.

The absorbed dose to the head for a 1100-MBq ^{99m}Tc source and a 42-min acquisition time was measured with an ionization chamber (Radcam, Capintec, Inc., Ramsey, NJ) at the center of a 160-mm diameter circular cylindrical plexiglass phantom. The absorbed dose was 0.1 mGy and is less than the 3.0 mGy absorbed dose to the head in a typical ^{99m}Tc-HMPAO study (44), and therefore will result in a trivial increase in the effective dose equivalent when a transmission study is acquired in addition to the SPECT brain study.

We have shown through computer simulation and experimentation that an optimally designed LSC can be used to produce transmission images of approximate isotropic resolution, approaching the intrinsic resolution of a scintillation camera. If the transmission images, which are automatically registered to the SPECT images, are incorporated into an iterative reconstruction algorithm with nonuniform attenuation correction (8), then improved quantification in brain SPECT with anatomical registration would be achieved.

APPENDIX

Derivation of the Geometric Efficiency of the LSC, G_{LSC}

The geometric efficiency of the LSC is equal to the product of the fractional solid angle of the LSC and the fraction of the line source unobstructed by the LSC. Assume the LSC septa have length l_{LSC} and thickness t_{LSC} and are separated by a distance s_{LSC}. For a point source, the elemental solid angle subtended by an element dx on the detector side of the LSC is

$$d\Omega_{LSC} = \frac{dA_\perp}{r^2} = \frac{(\cos\theta dx)s_{LSC}}{r^2},$$

where r is the distance from the point source to the element dx; $dA_\perp$ is the area of element dx perpendicular to the source; and θ is the angle between the normal of the LSC and the line of sight from the source to element dx. But $r = l_{LSC}/\cos\theta$ and $\cos\theta dx = rd\theta$, therefore, $dx = (l_{LSC}/\cos^2\theta)d\theta$.

Substituting,

$$d\Omega_{LSC} = \frac{s_{LSC}}{l_{LSC}}\cos\theta d\theta.$$

The solid angle is obtained by integrating over all θ:

$$\Omega_{LSC} = \frac{s_{LSC}}{l_{LSC}} \int_{-\pi/2}^{\pi/2} \cos\theta d\theta = 2\frac{s_{LSC}}{l_{LSC}}.$$

The fractional solid angle is:

$$\frac{\Omega_{LSC}}{4\pi} \text{ or } \frac{s_{LSC}}{2\pi l_{LSC}}.$$

The fraction of the line source unobstructed by the LSC is:

$$\frac{L_{OPEN}}{L_{UNIT}} = \frac{s_{LSC}}{s_{LSC} + t_{LSC}}.$$

Therefore, the geometric efficiency of the LSC, as described by Equation 1, is:

$$G_{LSC} = \frac{s_{LSC}}{s_{LSC} + t_{LSC}} \times \frac{s_{LSC}}{2\pi l_{LSC}}.$$

The computer simulations used to verify Equation 1 used a line source with a length equal to $10L_{UNIT}$.

REFERENCES

1. Sorenson JA. Quantitative measurement of radioactivity in vivo by whole body counting. In: Hine GJ, Sorenson JA, eds. *Instrumentation in nuclear medicine*. New York: Academic Press; 1974:311–348.
2. Chang LT. A method for attenuation correction in radionuclide computed tomography. *IEEE Trans Nucl Sci* 1978;25:638–643.
3. Gullberg GT, Budinger TF. The use of filtering to compensate for constant attenuation in single photon emission computed tomography. *IEEE Trans Biomed Eng* 1981;28:142–157.
4. Bellini S, Picenfini M, Cafforio C, Rocca F. Compensation of tissue absorption in emission tomography. *IEEE Trans Acoustics Speech Signal Process* 1979;27:213–218.
5. Tanaka E. Quantitative image reconstruction with weighted backprojection for single photon emission computed tomography. *J Comput Assist Tomogr* 1983;7:692–700.
6. Axelsson B, Israelsson A, Larsson SA. Studies of a technique for attenuation correction in single photon emission computed tomography. *Phys Med Biol* 1987;32:737–749.
7. Manglos SH, Jaszczak RJ, Floyd CE, Hahn LJ, Greer KL, Coleman RJ. Nonisotropic attenuation in SPECT: phantom tests of quantitative effects and compensation techniques. *J Nucl Med* 1987;28:1584–1591.
8. Tsui BMW, Gullberg GT, Edgerton ER, et al. Correction of nonuniform attenuation in cardiac SPECT imaging. *J Nucl Med* 1989;30:497–507.
9. Kemp BJ, Prato FS, Dean GW, Nicholson RL, Reese L. Correction for attenuation in technetium-99m-HMPAO SPECT brain imaging. *J Nucl Med* 1992;33:1875–1880.
10. Mazziotta J, Phelps M, Meadors A, Ricci A, Winter J, Benston J. Anatomic localization schemes for use in positron computed tomography using a specially designed headholder. *J Comput Assist Tomogr* 1982;6:848–853.
11. Bergstrom M, Boethius J, Eriksson L, Greitz T, Ribbe T, Widen L. Head fixation device for reproducible position alignment in transmission CT and PET. *J Comput Assist Tomogr* 1981;5:136–141.
12. Holman BL, Zimmerman RE, Johnson KA, et al. Computer-assisted superimposition of magnetic resonance and high-resolution technetium-99m-HMPAO and thallium-201 SPECT images of the brain. *J Nucl Med* 1991;32:1478–1484.
13. Pelizzari CA, Chen GTV, Spelbring DR, Weichselbaum R, Chen CT. Accurate three-dimensional registration of CT, PET and/or MRI images of the brain. *J Comput Assist Tomogr* 1989;13:20–26.
14. Maeda H, Itoh H, Ishii Y, et al. Determination of the pleural edge by gamma-ray transmission computed tomography. *J Nucl Med* 1981;22:815–817.
15. Malko JA, Van Heertum RL, Gullberg GT, Kowalsky WP. SPECT liver imaging using an iterative attenuation correction algorithm and an external flood source. *J Nucl Med* 1986;27:701–705.
16. Bailey DL, Hutton BF, Walker PJ. Improved SPECT using simultaneous emission and transmission tomography. *J Nucl Med* 1987;28:844–851.
17. Greer KL, Harris CC, Jaszczak RJ, et al. Transmission computed tomog-

18. Cao Z, Tsui BMW. Performance characteristics of transmission imaging using a uniform sheet source with parallel hole collimation. *Med Phys* 1992;19:1205–1212.
19. Manglos SH, Bassano DA, Duxbury CE, Capone RB. Attenuation maps for SPECT determined using cone beam transmission computed tomography. *IEEE Trans Nucl Sci* 1990;37:600–606.
20. Manglos SH, Bassano DA, Thomas FD. Cone-beam transmission computed tomography for nonuniform attenuation compensation of SPECT images. *J Nucl Med* 1991;32:1813–1820.
21. Manglos SH, Bassano DA, Thomas FD, Grossman ZD. Imaging of the human torso using cone-beam transmission CT implemented on a rotating gamma camera. *J Nucl Med* 1992;33:150–156.
22. Tung CH, Gullberg GT, Zeng GL, et al. Nonuniform attenuation correction using simultaneous transmission and emission converging tomography. *IEEE Trans Nucl Sci* 1992;39:1134–1143.
23. Gullberg GT, Malko JA, Eisner RL. Boundary determination methods for attenuation correction in single photon emission computed tomography. In: Esser PD, ed. *Emission computed tomography: current trends*. New York: The Society of Nuclear Medicine; 1983:33–53.
24. Jaszczak RJ, Gilland DR, Hanson MW, et al. Fast transmission CT for determining attenuation maps using a collimated line source, rotatable air-copper-lead attenuators and fan-beam collimation. *J Nucl Med* 1993;34: 1577–1586.
25. Kemp BJ, Prato FS, Reese L. Transmission CT of the head with a SPECT system equipped with a collimated line source and a fan-beam collimator. *Radiology Suppl* 1992;185:251–252.
26. Kemp BJ, Prato FS, Reese L. Transmission imaging with a SPECT system and a collimated line source [Abstract]. *J Nucl Med* 1994;35:92P.
27. Tan P, Bailey DL, Meikle SR. A scanning line source for simultaneous emission and transmission measurements in SPECT. *J Nucl Med* 1993;34: 1752–1760.
28. Glover GH, Pelc NJ. Nonlinear partial volume artifacts in x-ray computed tomography. *Med Phys* 1980;7:238–248.
29. Beck JW. Analysis of a camera based SPECT system. *Nucl Instr Meth* 1983;213:415–436.
30. Mather RL. Gamma-ray collimator penetration and scattering effects. *J Appl Phys* 1957;28:1200–1207.
31. *NIST x-ray and gamma ray attenuation coefficient and cross-section database*, Version 2.0. Gaithersburg, MD: US Department of Commerce, National Institute of Standards and Technology, Standard Reference Data Program.
32. Judy PF. The line spread function and modulation transfer function of a computed tomographic scanner. *Med Phys* 1976;3:233–236.
33. Cunningham IA, Fenster A. A method for modulation transfer function determination from edge profiles with correction for finite-element differentiation. *Med Phys* 1987;14:533–537.
34. Cunningham IA, Reid BK. Signal and noise in modulation transfer function determinations using slit, wire, and edge techniques. *Med Phys* 1992;19: 1037–1044.
35. Barrett HH, Swindell W. *Radiological imaging–the theory of image formation, detection and processing*. New York: Academic Press; 1981:608–610.
36. Gullberg GT, Crawford CR, Tsui BMW. Reconstruction algorithm for fan beam with a displaced centre-of-rotation. *IEEE Trans Med Imag* 1986;5:23–29.
37. Yester MV, Barnes GT. The geometrical limitations of CT scanner resolution. *Proc SPIE* 1977;127:296–303.
38. Johns PC, Yaffe M. Scattered radiation in fan beam imaging systems. *Med Phys* 1982;9:231–239.
39. Lederer CM, Hollander JM, Perlman I. *Table of isotopes*. New York: John Wiley and Sons, Inc.; 1967:571.
40. White DR, Widdowson EM, Woodard HQ, Dickerson JWT. The composition of body tissues. *Br J Rad* 1991;64:149–159.
41. AAPM Report No. 39. *Specification and acceptance testing of computed tomography scanners*. New York: American Institute of Physics, Inc.; 1993.
42. Barrett HH, Swindell W. *Radiological imaging–the theory of image formation, detection and processing*. New York: Academic Press; 1981:136.
43. Anger HO. Scintillation camera with multichannel collimators. *J Nucl Med* 1964;5:515–531.
44. Neirinckx RD, Canning LR, Piper IM, et al. Technetium-99m d,l-HMPAO: a new radiopharmaceutical for SPECT imaging of regional cerebral blood perfusion. *J Nucl Med* 1987;28:191–202.